Multiphysics Simulation of Thermal-Fluid Behavior in Laser Powder Bed Fusion of H13 Steel: Influence of Layer Thickness and Energy Input

Patiparn Ninpetch[1] · **Prasert Chalermkarnnon**[2] · **Pruet Kowitwarangkul**[1]

Abstract

In this research, the multiphysics modelling was implemented for laser powder bed fusion (L-PBF) process simulation to study the influence of layer thickness on thermo-fluid behavior, and single tracks formation during L-PBF process of AISI H13 steel. The influence of energy input adjustment on forming characteristics of single tracks in various layer thickness were examined and predicted in this work. The discrete element method and the computational fluid dynamic model were implemented to simulate the temperature distribution, and molten metal flow behavior during L-PBF process. The results indicated that the layer thickness has more effect on the depth of single track than width of single track. Due to high thermal conductivity between solid substrate and powder bed at the lowest layer thickness of 30 μm, the shallowest single tracks penetration depth was formed. The adjustment of energy input including laser power and scanning speed is an effective method to obtain the sufficient depth of penetration at 30 μm, 70 μm, and 100 μm layer thicknesses. The single track depth with the layer thicknesses of 30 μm reduced around 27 μm when laser power was decreased from 200 to 125 W and 28 μm and the scanning speed was increased from 1000 to 1600 mm/s. At 70 μm layer thickness the depth of single track was increased around 20 μm when the laser power was elevated from 200 to 250 W, and 19 μm when scanning speed was reduced from 1000 to 800 mm/s. Moreover, from this study the numerical simulation result revealed the layer thickness adjustment range between 50 and 70 μm with particle sizes used in this research provided the single track with continuous, regular sizes and sufficient penetration depth when medium energy density is used.

Keywords Additive manufacturing · Laser powder bed fusion · Numerical modelling · Thermal behavior · H13 tool steel

1 Introduction

H13 tool steel is hot work tool steel that is generally used in the manufacturing of molds and dies for hot metal processes due to its high wear resistance, toughness, and hardness at elevated temperature [1–3]. The main application of H13 steel is injection molds with conformal cooling channels, which is typically used in plastic injection molding process for the improvement of heat dissipation, uniform cooling, tool life, and higher productivity [4]. Although the mold with conformal cooling channels parts has intricate structures which are difficult to be manufactured by traditional manufacturing processes [5, 6]. For overcoming this issue, the laser powder bed fusion (L-PBF) process becomes the promising manufacturing technology for fabrication the component with elaborate structure [2, 7]. L-PBF process is a metal additive manufacturing technology that uses a laser source as a moving heat energy to selectively melt and fuse the metallic powder in layer-by-layer fashion according to three-dimensional CAD models [8–10]. This process has ability to produce metallic components with complex geometries with various applications such as medical devices, automotive, aerospace, energy, and molds manufacturing [11–13]. Moreover, the process can manufacture metal parts with nearly full density and good mechanical properties in numerous metallic materials such as tool steels, titanium alloys, stainless steels, cobalt chrome alloys, and aluminuim alloys [14, 15]. In general, the L-PBF process involves several complicated physics including heat transfer, fluid flow,

✉ Pruet Kowitwarangkul
 pruet.k@tggs.kmutnb.ac.th

1 The Sirindhorn International Thai-German Graduate School of Engineering (TGGS), King Mongkut's University of Technology North Bangkok, Bangkok 10800, Thailand

2 Assistive Technology and Medical Devices Research Center, National Science and Technology Development Agency, Pathum Thani 12120, Thailand

phase transition, material evaporation, and the Marangoni effect among other etc. [16–18]. The occurrence of these physics has a considerable influence on underlying physical phenomena such as thermal behavior, melt pool dynamics, the evolution of molten pool, and defects formation e.g., porosity, humping effect, balling effect, keyholing, cracking. These defects are detrimental effects on the quality of as-built products such as low relative density, poor surface quality, inferior mechanical properties, and low building efficiency [8, 19]. In addition to complicated physics, the physical phenomena in L-PBF process significantly depends on the determination of processing parameters [20, 21] such as laser power (P), scanning speed (v), laser spot size (L_s), hatch spacing (H), layer thickness (L_t), linear energy density (LED) (ratio between power of laser source and scanning velocity).

Insightful understanding in the physical phenomena during L-PBF process can help to improve build quality and prevent the defects formation. Nonetheless, since the physical phenomena takes place at micro levels with a very short period, the investigation and observation of physical phenomena by experimental method are relatively difficult [21–23]. Therefore, the Multiphysics modelling for L-PBF process is a powerful tool to examine the effects of process parameters on physical phenomena [14, 22, 24]. Additionally, the models can provide a better understanding on the physical mechanisms. Over recent year, many research studies have been developed and applied the Multiphysics modelling to examine the physical phenomena, and the influence of process parameters on single track formation and defects formation during L-PBF process [25–29]. For instance, Cao [30] studied the effect of laying powder on single track formation by using numerical modelling. It was discovered that the metal powder with small size can be used to acquire the good formation zone. Panwisawas et al. [31] established a numerical model of SLM process to investigate the influence of layer thickness and scanning speed on the scanning tracks morphology of Ti-6Al-4 V by using thermal fluid dynamics calculations. The findings indicated that when the higher laser scanning speed and layer thickness are applied, the solidified track becomes irregular shapes. Wu et al. [32] developed the numerical model of SLM process of H13 to investigate the effect of evaporated metal and recoil pressure on the molten pool. They discovered that the wider molten pool was formed during the neglecting evaporation. Furthermore, the author [22] implemented the Multiphysics modelling to analyze the effect of laser power and scanning speed on single track formation in L-PBF process of H13 tool steel. The layer thickness of powder bed was 50 μm. The result revealed that the single track with uniform and deep penetration depth can be generated with laser power and scanning speed of 200 W and 1000 mm/s.

For industrial production, the building rate of L-PBF process is relatively low, resulting in the low productivity [33, 34]. One of the methods to increase the building rate in L-PBF process is an increasing of the layer thickness of powder bed [35]. Meanwhile, the decreasing of layer thickness can generally improve surface roughness of final built component. However, when the layer thickness is adjusted, there are significant effects on the thermal behavior, melt pool dynamics, and scanning track formation. Therefore, it is necessary to investigate the effects of layer thickness on the thermal behavior, and scanning track formation in L-PBF process. Since the quality of final build parts fabricated by L-PBF process depends on the single track forming, this research focuses on investigation of the single track formation. The formation of single tracks with continuous, uniform, and sufficient penetration depth are necessary in L-PBF process to manufacture the build component with high relative density and good metallurgical bonding [36].

Therefore, in the current research, the meso-scale Multiphysics modelling was implemented to examine the influence of layer thickness on thermal behavior, molten pool dynamics, and single tracks formation during L-PBF process of H13 tool steel. The influence of energy input adjustment including laser power, and scanning speed on forming characteristics of single tracks in various layer thickness were investigated and predicted. The discrete element method and computational fluid dynamics (DEM-CFD) model for L-PBF process were employed to establish the powder spreading upon the solid substrate plate and simulate the temperature distribution, molten metal flow behavior, and forming characteristics of scanning track. A moving heat source on the top of the powder bed layer was calculated by a moving Gaussian heat source model. The findings obtained from this research provides scientific guidance on the selection and determination of processing parameters in L-PBF process to produce effective final parts with high relative density and defects free of AISI H13 steel components.

2 Numerical Model

2.1 Powder Bed Generation Model

To generate metal particle bed on solid substate, the discrete element method (DEM) was implemented to model the movement of particles including particles to particles and particles to wall interactions. The metal particles in this study were defined as perfect spherical shape with different radius. Moreover, the wall and substrate were also set as rigid. The individual metal particle velocities in x, y, z directions including translational and rotational components was calculated by DEM to solve the Newton's second law

of motion. The particle-to-particle models are shown in Eqs. (1)–(3) [37, 38]:

Particle interaction force in normal direction:

$$\mathbf{F_{ni}} = -k_s \, dl\mathbf{n} - \eta_n(\mathbf{u'n})\mathbf{n} \tag{1}$$

Particle interaction force in tangential direction:

$$\mathbf{F_{ti}} = -\eta_t(\mathbf{u'} - (\mathbf{u'\,n})\mathbf{n}) \tag{2}$$

Total particle interaction force:

$$\mathbf{F_i} = \mathbf{F_{ni}} + \mathbf{F_{ti}} = -\mathbf{F_j}$$
$$l_0 = r_i + r_j; \mathbf{I} = \mathbf{x_j} - \mathbf{x_i}; \, dl = l_0 - \|\mathbf{I}\|; \mathbf{n} = \frac{\mathbf{I}}{\mathbf{I}}; \mathbf{u'} = \mathbf{u_j} - \mathbf{u_i} \tag{3}$$

where x_i is a coordinate vector of an individual particle center, r_i is particle radius, k_s is spring constant, u_i is particle velocity vector, and η is drag coefficient.

2.2 Thermo-Fluid Model

L-PBF process involves complex physics such as heat transfer, molten metal flow, and phase transformation. These complex physics can mainly be solved by using computation fluid dynamic (CFD) model based on conservation equations of mass, energy, and momentum as shown in Eqs. (4)–(6) [39–41]:

Mass: $\nabla. \vec{v} = 0$ (4)

Energy: $\dfrac{\partial h}{\partial t} + \left(\vec{v} \cdot \nabla\right)h = -\dfrac{1}{\rho}(\nabla.k\nabla T) + \dot{q}$ (5)

Momentum: $\dfrac{\partial \vec{v}}{\partial t} + \left(\vec{v} \cdot \nabla\right)\vec{v} = -\dfrac{1}{\rho}\nabla P + \mu\nabla^2 \vec{v} + \vec{g} + F_b$ (6)

where $\vec{v}$ is the velocity of melted metal, P is the pressure, ρ is density, μ is kinetic viscosity, g is gravity force, F_b is the body force in the system, h is enthalpy, k is thermal conductivity, T is temperature, $\dot{q}$ is heat source term, and t is time. The molten fluid flow in melt pool was considered to be Newtonian fluid, incompressible, and laminar flow.

Moreover, molten pool surface morphology was reconstructed and precisely captured by the volume of fluid (VOF), which computational method to simulate the evolution of free surface as presented in Eq. (7) [25–42]:

$$\frac{\partial F}{\partial t} + \nabla \cdot (\vec{v}F) = 0 \tag{7}$$

A cell is void when F = 0, and completely occupied by the fluid when F = 1. When the value of F is between 0 and 1, an interface between the fluid and void exists in the cell.

Marangoni effect is the phenomena of mass transfer along the molten pool surface because of the temperature gradient. The Marangoni effect and surface tension have considerable influence the surface morphology of molten pool, heat convection inside the molten pool during cooling, and scanning track characteristic. The surface tension model with temperature dependent is presented in Eq. (8) [22, 37]:

$$\gamma(T) = \gamma_o + \frac{d\gamma}{dT}\left(T - T_m\right) \tag{8}$$

where γ is the surface tension at temperature, γ_o is the surface tension at melting temperature, T_m is melting temperature, and $\frac{d\gamma}{dT}$ is surface tension coefficient with temperature dependent.

2.3 Phase Transition and Material Evaporation

To numerically consider the phase transformation between the solid phase and liquid phase, the latent heat of fusion model was utilized. Additionally, the temperature within laser center region exceeds the boiling point of materials. As a result, the recoil pressure caused by metal evaporation takes places over the molten metal surface. The enthalpy equation and recoil pressure equation are expressed in Eqs. (9) and (10) [37, 43, 44]:

$$h = \int C_p dT + L_f f \tag{9}$$

$$P_r = 0.54 P_o exp\left(\Delta H_v \frac{T - T_b}{RTT_b}\right) \tag{10}$$

where h is enthalpy, C_p is specific heat, L_f is latent heat of fusion, f is the volumetric fraction of liquid with temperature dependent, ΔH_v is the enthalpy of metal vapor, P_0 is the saturation pressure, R is gas constant, and T_b is boiling temperature of material.

2.4 Laser Heat Source Model

The Gaussian heat source model, which is a moving heat flux, was defined on the top of the powder bed layer. The equation is described as below [22, 45, 46]:

$$Q_{Laser} = \frac{\eta P_{Laser}}{\pi R_s} exp\left(-2\frac{\left(x - x_s\right)^2 + \left(y - y_s\right)^2}{R_s^2}\right) \tag{11}$$

Fig. 1 Computational domain
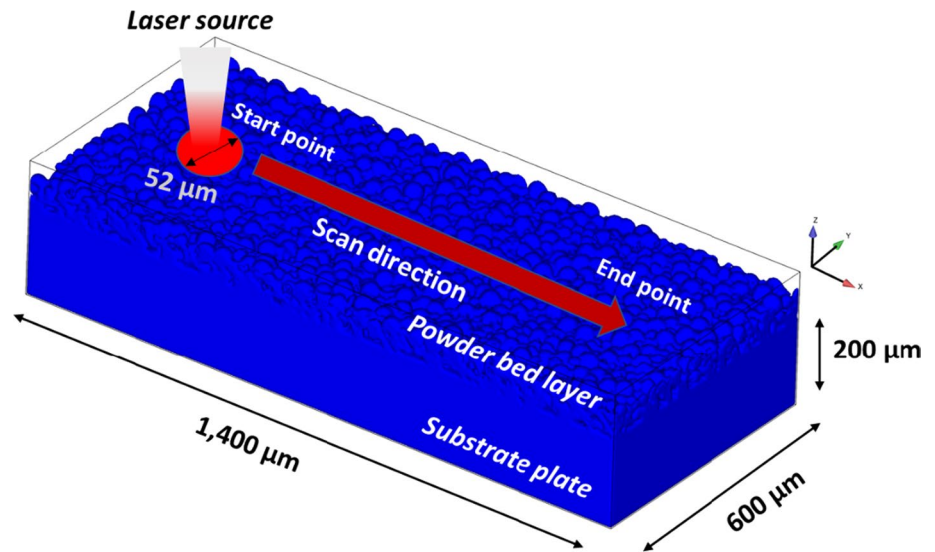
where Q_{Laser} is the surface heat flux, η is the absorption coefficient, P_{Laser} is the laser power, R_s is the laser diameter, x_S, and y_S are the coordinates of the laser beam center.

2.5 Numerical Simulation Configuration

A mesoscale Multiphysics modelling was performed by using CFD simulation software FLOW-3D/ FLOW-AM. The setup of numerical modelling begins with the preparation of the metal powder bed layer CAD model by using FLOW-DEM software to obtain the STL CAD file. Then, the STL file of metal particle bed was uploaded to the CFD simulation software FLOW-AM to simulate the temperature distribution, fluid flow behavior, Marangoni effect, and scanning track characteristics during L-PBF process. Figure 1 illustrates computational domain. The mesh elements of three million cells with the size of 4.5 μm were defined for all computational domain, which have been proven to provide reasonable numerical result [22]. The void region above the metal powder layer was imposed as atmospheric pressure and initial temperature of 298 K. The particle size distributions (PSD) of H13 tool steel with spherical shape in this study were D10 (19 μm), D50 (29 μm), and D90 (43 μm) [32]. The particle filling rate of all cases were around 61%. The substrate material was H13 steel.

2.6 Material Properties and Processing Parameters

The thermal-physical properties of H13 used in this study are tabulated in Table 1 [22, 32, 37]. To investigate the thermal behavior and the formation of single tracks, Table 2 shows the processing parameters including laser powers, scanning speeds, LED, and layer thicknesses. The laser spot size was 52 μm.

Table 1 Material properties used in the simulation [22, 32, 37]

Material properties	Value
Solidus temperature	1588 K
Liquidus temperature	1727 K
Boiling temperature	3133 K
Thermal conductivity	29 W/mK
Specific heat	460 J/kgK
Latent heat of fusion	2.5×10^5 J/kg
Latent heat of evaporation	7.34×10^6 J/kg
Surface tension	1.7 N/m

Table 2 Processing parameters for ten case studies

Case studies	Laser power (W)	Scanning speed (mm/s)	Linear energy density (J/mm)	Layer thickness (L_t) (μm)
A1	200	1000	0.2	30
A2	200	1000	0.2	50
A3	200	1000	0.2	70
A4	200	1000	0.2	100
B1	125	1000	0.125	30
B2	200	1600	0.125	30
B3	250	1000	0.25	70
B4	200	800	0.25	70
B5	400	1000	0.4	100
B6	200	500	0.4	100

Fig. 2 The comparison of molten pool width and depth between the numerical modelling of this current study and experiment reported by Wu et al. [32]
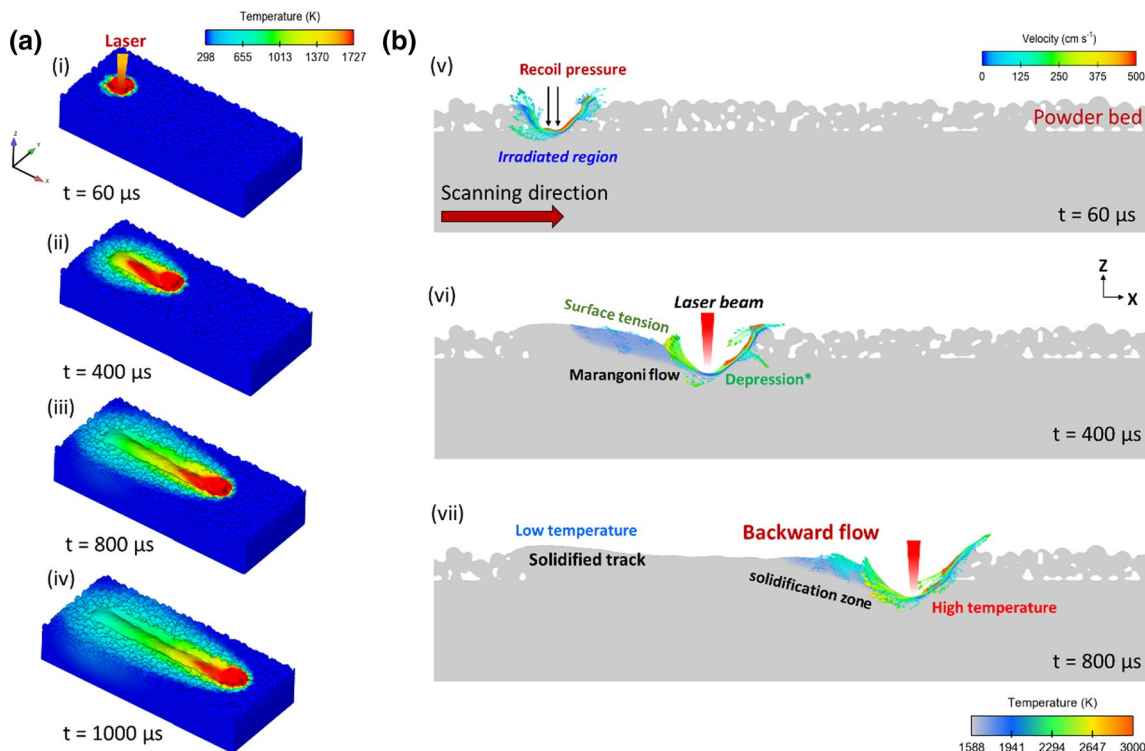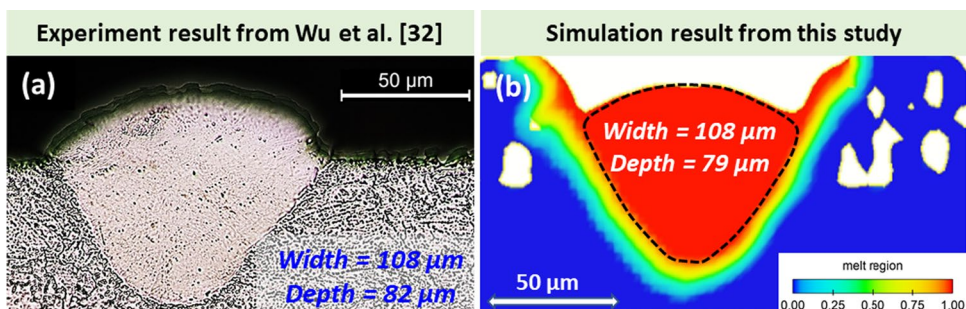

Fig. 3 Temperature distribution at different times with laser power of 200 W, scanning speed of 1000 mm/s, LED of 0.2 J/mm, and layer thickness of 50 μm (**a**) and molten metal flow and velocity flow field (**b**)

3 Result and Discussions

3.1 Numerical Modelling Validation

To verify the accuracy of the numerical model of the present study, the numerical model was validated with the experimental result of single track formation reported by Wu et al. [32]. The dimensions of molten pool width and depth obtained from numerical model were compared to the experimental study. Figure 2 illustrates the comparison of molten pool width and depth between the numerical modelling of this current study and experiment reported by Wu et al. [32]. The molten pool boundary of simulation is displayed in red color and blue color represents the solid region. It can be noticed that the numerical result agreed

with the experimental result. Hence, it can be applied for the investigation in this study.

3.2 Temperature Distribution and Molten Metal Dynamics

Figure 3a shows the numerical modelling result of temperature distribution during L-PBF process at different times with laser power of 200 W, scanning speed of 1000 mm/s, LED of 0.2 J/mm, and layer thickness of 50 μm. At the beginning, when the laser heat source collided on the powder bed, the temperature distribution with round shape was formed. As laser source proceeds along the scanning direction, the shape of temperature distribution on metal powder bed layer can be changed from round shape to elliptical
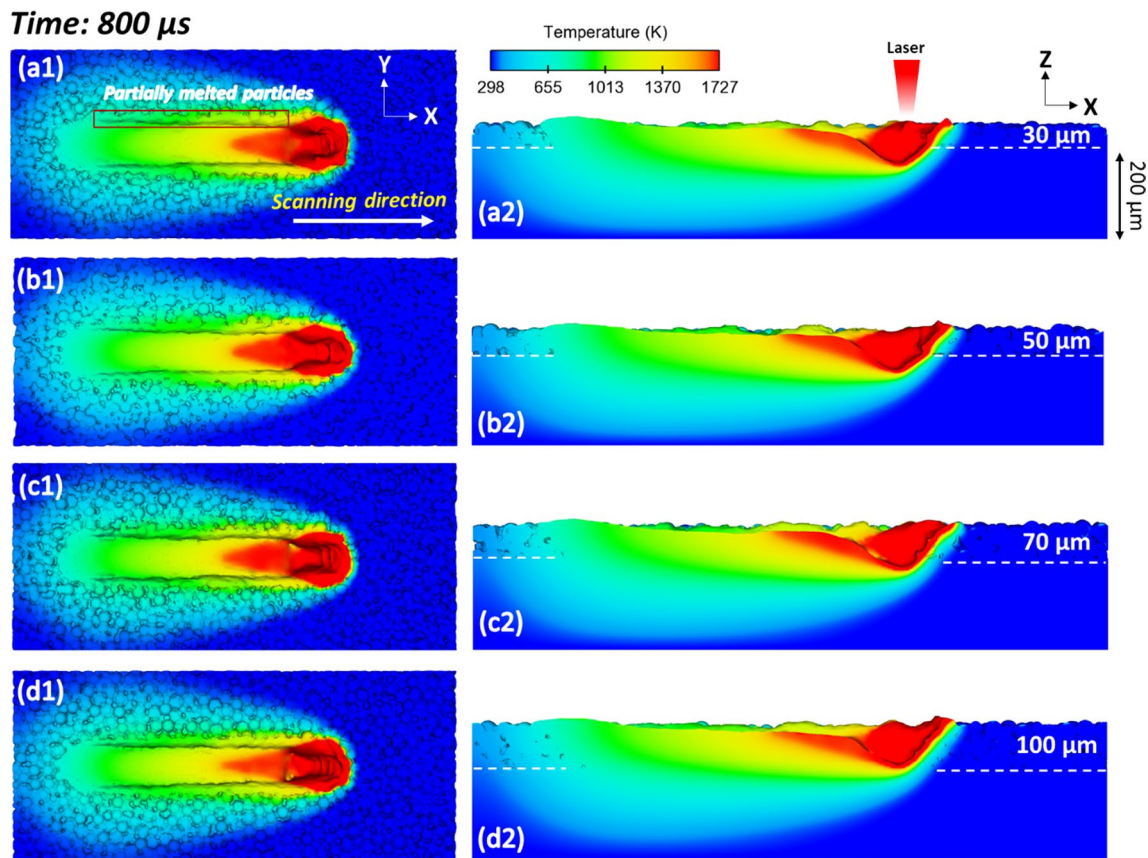
Fig. 4 Temperature distribution of powder bed at four different layer thicknesses

shape and then form comet-like shape at the tail of comet shape has pointed opposite to the laser scanning direction as exhibited in Fig. 3a(ii). Then, the comet-shape area of the temperature distribution was expanded because of the heat accumulation in powder bed layer and solid substrate plate. Figure 3b shows the flow characteristic of molten metal and velocity flow field in L-PBF process. At the beginning of the process, the metal particles were melted and fused by heat from laser source to generate the molten pool. The molten pool was depressed by gasification recoil force induced by evaporated metal as shown in Fig. 3b(v). The molten metal on the molten pool surface rearward flowed from the center of irradiated zone with high temperature to the tail of the molten pool with low temperature as shown in direction of flow velocity vector (see in Fig. 3b(vi)). This is because of Marangoni effect that happens on the molten metal surface caused by the surface tension gradient. Then, when the laser beam moving forward, the temperature of the tail of molten pool was gradually decreased. When the temperature is below the solidus temperature of 1588 K, the molten pool starts to solidify and originate the solidified track because of heat dissipation, and heat accumulation as shown in Fig. 3b(vii).

3.3 Influence of Layer Thickness on Thermal Behavior

Figure 4 demonstrates the simulation results of temperature distribution of powder bed at four different layer thicknesses: (a) 30 μm (A1), (b) 50 μm (A2), (c) 70 μm (A3), and (d) 100 μm (A4). The distribution of temperature is represented by color contour. The laser power, scanning speed and LED in the analysis were considered as 200 W, 1000 mm/s, and 0.2 J/mm. The simulation results revealed that the temperature distribution region along Y-axis and Z-axis directions in all layer thickness cases were insignificant different as shown in Fig. 4a1–d1, a2–d2.

The temperature variation during the L-PBF process under four different layer thickness of 30 μm, 50 μm, 70 μm, and 100 μm is illustrated in Fig. 5. To observe and collect the temperature data, the probes A and B were attached at the middle of the powder layer and top layer of substrate of each case as shown in Fig. 5a. As illustrated in Fig. 5b, The temperature peak took place when the laser beam passed the probe A, the temperature increased rapidly and then suddenly undetected by showing the room temperature of 298 K because the probe was not contact with the molten metal of melt pool due to the depression of molten pool.

Fig. 5 Temperature variation during the L-PBF process at four different layer thicknesses; **a** sectional view, **b** probe A, and **c** probe B
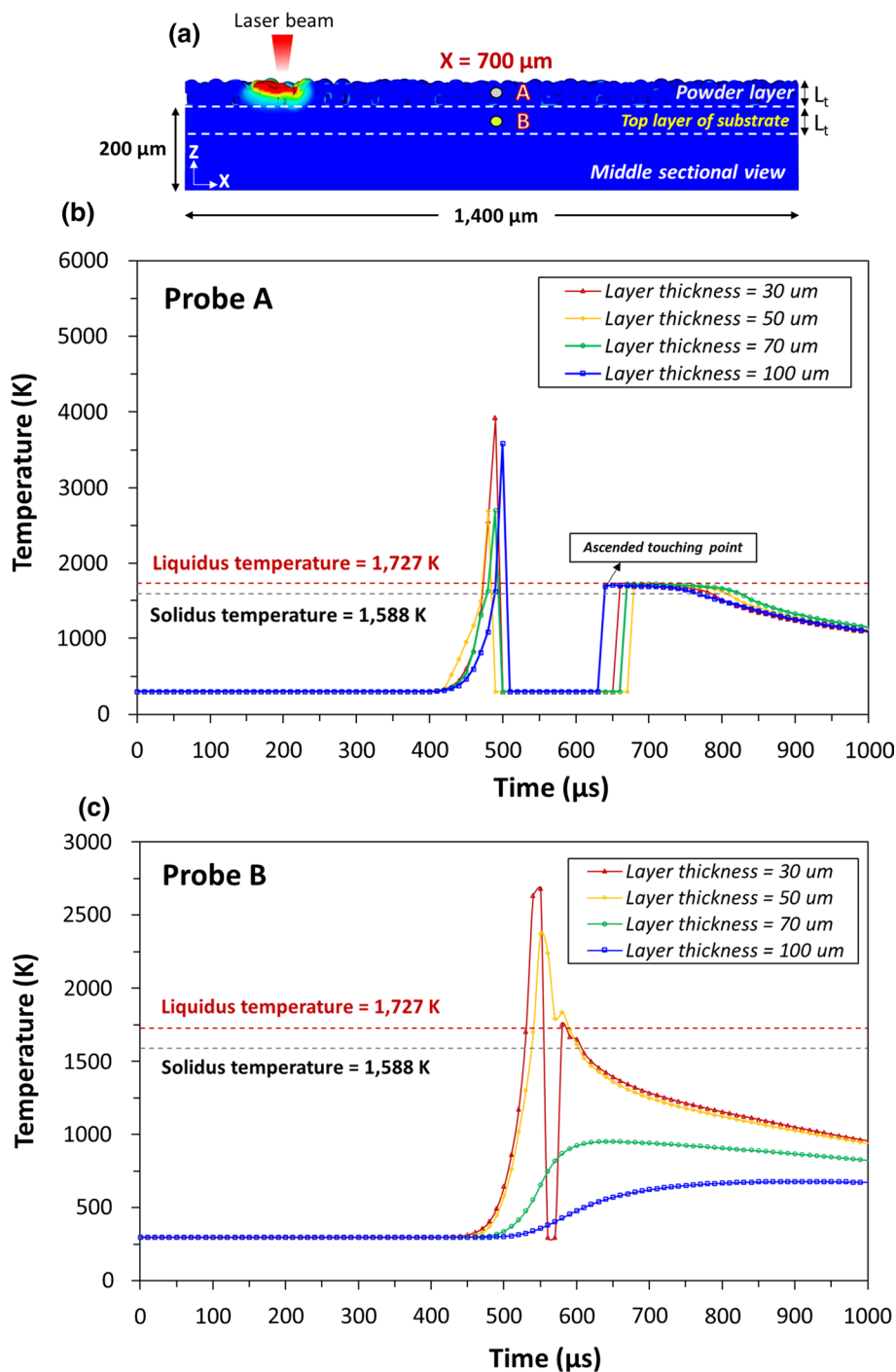
Then, the temperature was detected again when the melt pool was cooling down and the molten metal of melt pool surface ascended through the probe A. The start time of the ascended touching point of layer thickness of 30 μm, 50 μm, 70 μm, and 100 μm cases were around 660 μs, 680 μs, 670 μs and 640 μs respectively. The start time of the ascended touching point of the case with layer thickness of 100 μm is earlier than the other cases due to the shortest distance between probe and bottom of the molten pool. The start time

of other cases are nearly the same with minor differences due to other factors such as the different level of molten pool bottom and the variation of heat conduction and molten flow dynamics.

Additionally, the peak temperature at the probe point B of layer thicknesses of 30 μm, 50 μm, 70 μm, and 100 μm were 2685 K, 2371 K, 954 K, and 679 K respectively as exhibited in Fig. 5c. It can be observed that the temperature at probe B of layer thickness of 30 μm and 50 μm cases exceed the
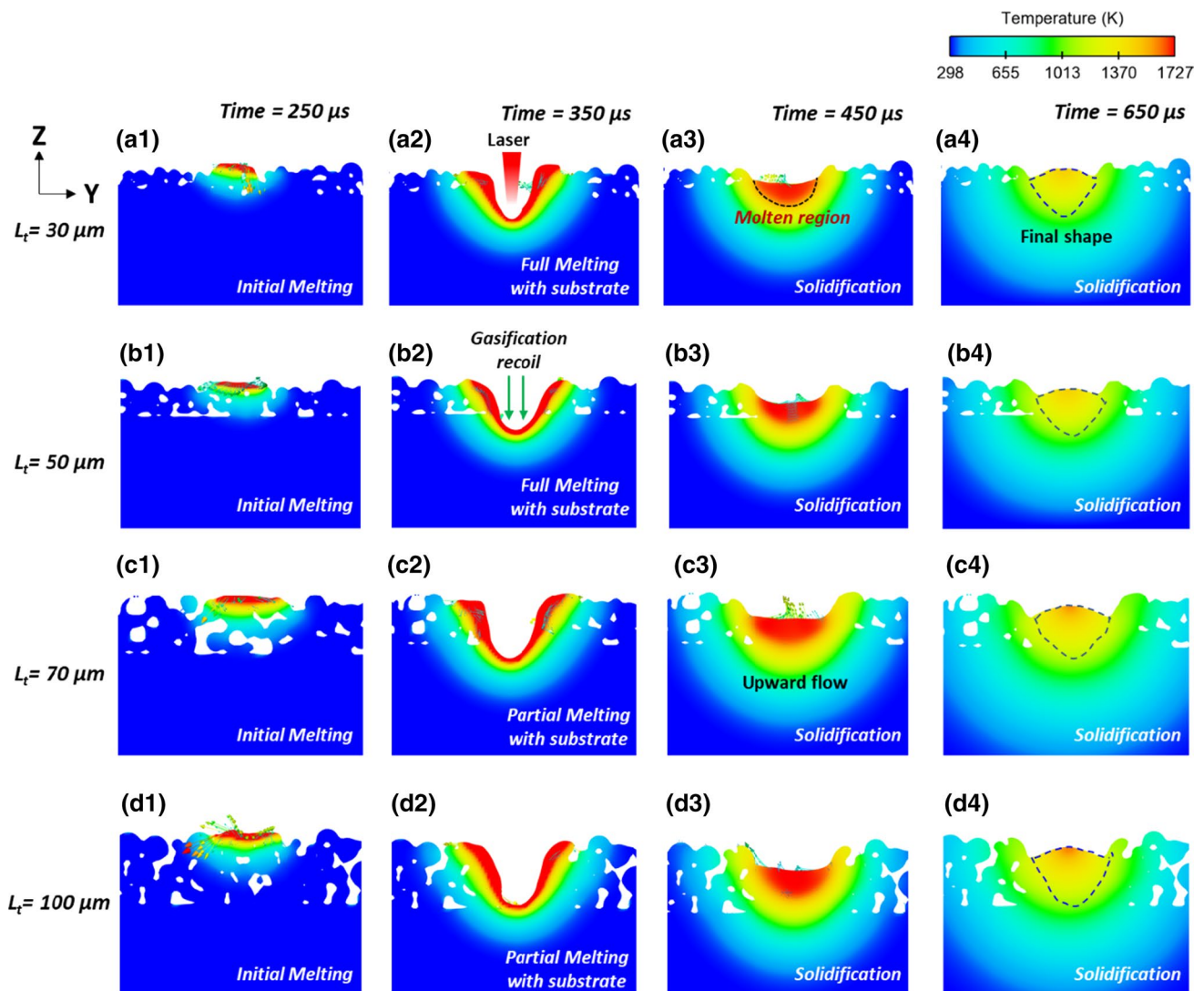
Fig. 6 The evolution of molten pool at monitoring section view x = 500 μm at four different layer thicknesses

melting temperature of H13 (1700 K). This indicated that the molten metal can flow to probe point B position, as a result, the full melting between powder bed and substrate can be obtained. On the other hand, at the higher layer thickness of 70 μm and 100 μm, the temperature at probe point B was lower than melting temperature of material. Consequently, the probe point B region of these conditions was still in solid state due to inadequate energy density from laser source to melt the powder bed and substrate plate.

3.4 Influence of Layer Thickness on Molten Pool Evolution and Single Tracks Formation

Figure 6 demonstrates the evolution of molten pool at section view plane x = 500 μm at four different thickness of powder layer cases A1-A4. Four cases with layer thickness of 30 μm (A1), 50 μm (A2), 70 μm (A3), and 100 μm (A4)

were chosen for the study. The laser power, scanning speed, and LED applied in the analysis were 200 W, 1000 mm/s, and 0.2 J/mm respectively. As shown Fig. 6a1–d1, the metal powders bed was initially melted and agglomerated while the partial laser beam reaches at observed section plane. At 350 μs, the metal powder was completely melted when the laser heat beam continuously moves to the observed section plane. The molten metal downward flows to form the molten pool depression due to the formation of gasification recoil pressure at the melt pool surface as illustrated in Fig. 6a2–d2. Moreover, the numerical results indicated that when layer thickness of 30 μm, and 50 μm were applied, the heat energy from laser source can be readily transferred from the top surface of powder bed layer to bottom surface and substrate plate. As a result, the full melting between metal powder bed and solid substrate were formed as shown in Fig. 6a2, b2. Meanwhile, the partial melting of metal powder
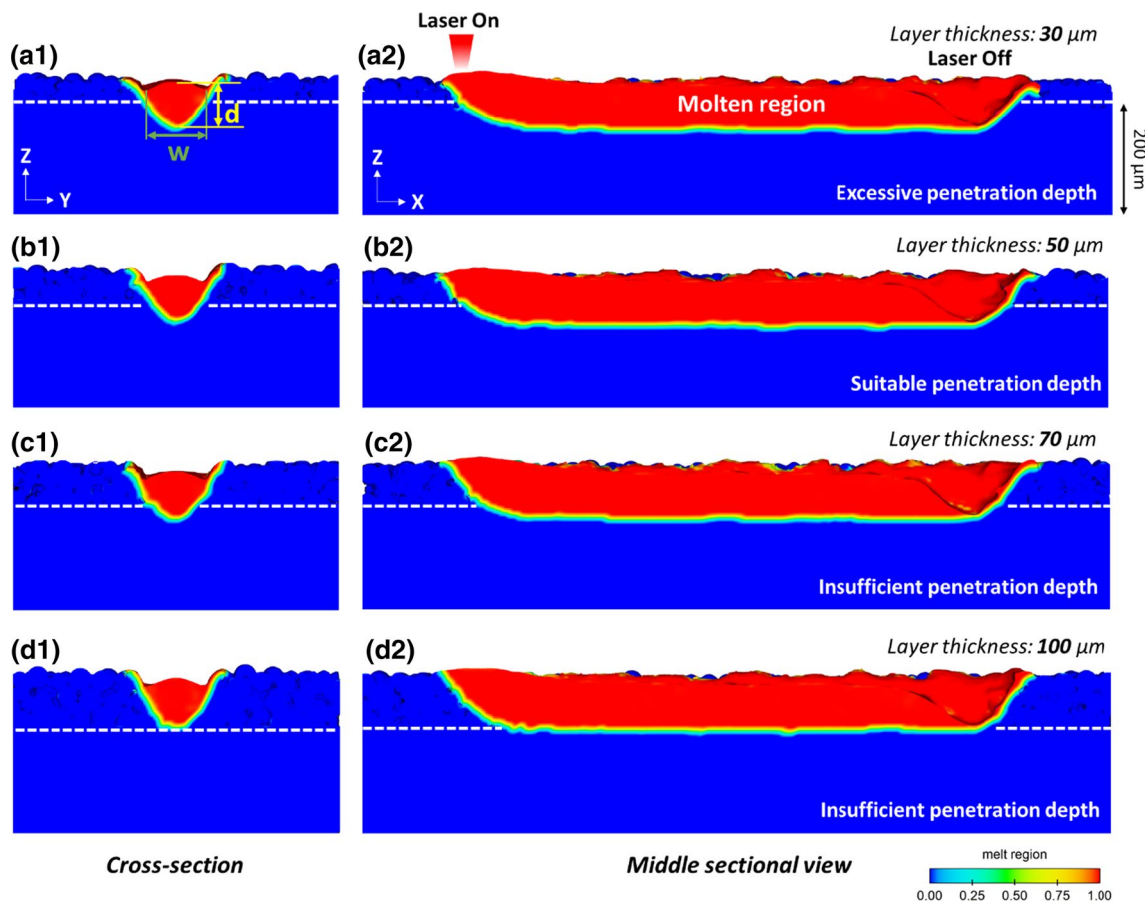
Fig. 7 Single tracks formation at four different layer thicknesses with laser power of 200 W, scanning speed of 1000 mm/s, and LED of 0.2 J/mm

bed with substrate was generated with layer thickness of 70 μm, and 100 μm which resulted in weak metallurgical bonding between powder bed and substrate plate. The weak metallurgical bonding between powder layers contributed to the defect formation such as void, lack of fusion, and balling effect. These defects are not desirable and should be avoided in the L-PBF production. At 450 μs, as laser beam moves away from observed section plane, the molten pool evolution entered solidification stage. The molten metal tended to solidify from the bottom to top. The flow direction of molten metal was changed from downward direction to upward direction for gap filling of molten pool as the gasification recoil pressure was released as displayed in Fig. 6a3–d3. At the progress time of 650 μs, the molten pool evolution process of all case was almost completely solidified and transformed to cooling stage. It can be observed that the molten pool with layer thickness of 30 μm and 50 μm was solidifier than high layer thickness cases because of high thermal conductivity, high thermal dissipation and low heat accumulation between solidified powder layer and solid substrate. Since the formation of interfacial force including surface tension, and Marangoni effect caused by temperature

gradient inside the molten pool, the final molten pool with convex surface morphology was generated. It was also found that the final molten pool shape of all layer thickness cases was relatively similar with minor difference as presented in Fig. 6a4–d4. The final shape of molten pool is exhibited as blue dash-dotted lines. The insight understanding of evolution molten pool during L-PBF process is essential to govern the final build products quality such as microstructure evolution, mechanical properties, and defects.

The simulation results of the formation of single tracks at four different layer thicknesses with laser power of 200 W, scanning speed of 1000 mm/s, and LED of 0.2 J/mm are shown in Fig. 7. The molten pool region and solid region in this model are represented as red color and blue color region consecutively. The single track formation conducts along scan direction of laser heat source. From the cross-sectioning view as shown in Fig. 7a1–d1, the scanning tracks with a semicylindrical shape occurred in all layer thickness cases. Similarly, from the middle sectioning view, the single tracks with continuous and regular size formed in all layer thickness conditions as exhibited in Fig. 7a2–d2. As illustrated in Fig. 8, the final solidified track morphology with continuous

Fig. 8 Final solidified track morphology of single track at four different layer thicknesses with laser power of 200 W, scanning speed of 1000 mm/s, and LED of 0.2 J/mm
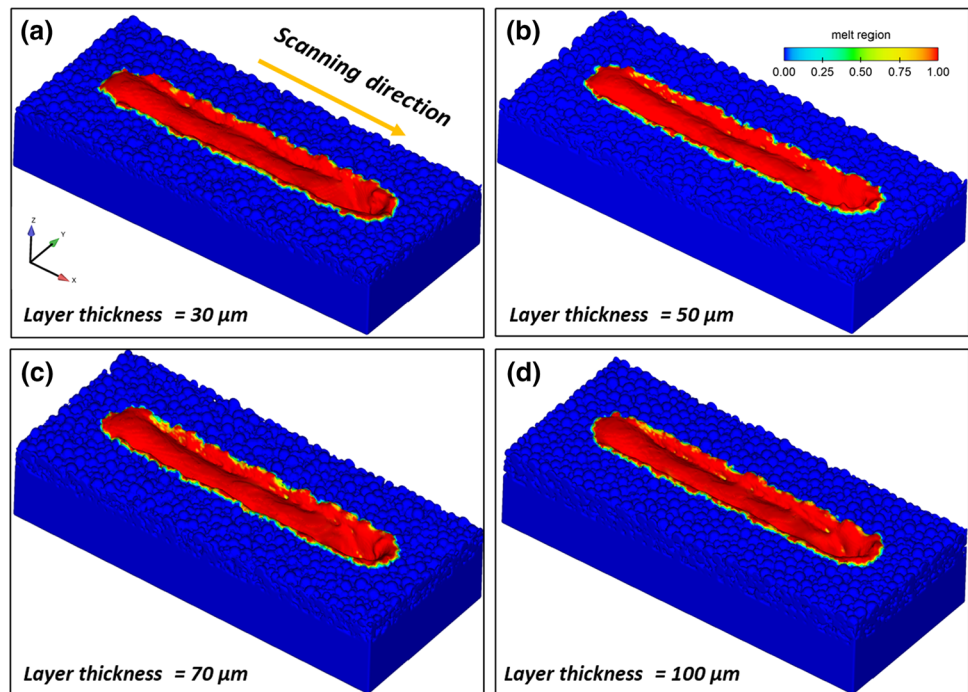
and smooth tracks can be generated in all layer thickness cases. This indicated that the sufficient of energy density was applied in all layer thickness cases. Table 3 presents the geometric dimensions of single tracks tracks including width (w) and depth (d) obtained from numerical modelling. The width and depth dimensions of single tracks were obtained from average of measurement data at the cross sections of 0.6 mm, 0.7 mm, and 0.8 mm along scanning direction. The w and d dimensions with layer thickness of 30 µm, 50 µm, 70 µm, and 100 µm were 105 and 76 µm, 108 µm and 79 µm, 105 µm and 79 µm, and 106 µm and 81 µm respectively. From the result, it can be found that the layer thickness has more impact on the single track depth (d) than single track width (w). Moreover, the shallowest depth of penetration single tracks took place with the lowest layer thickness of 30 µm because the heat energy was easily transferred to solid substrates plate, which high thermal conductivity. The depths of single tracks (d) in all layer thickness obtained from laser power of 200 W, scanning speed of 1000 mm/s, and LED of 0.2 J/mm were around 76 to 81 µm, which was equivalent to two layers melted beneath at layer thickness of 30 µm case. As a result, the single track with excessive

penetration depth was generated as displayed in Fig. 7a2. Meanwhile, at the layer thickness of 50 µm, the single track with sufficient penetration depth was formed as illustrated in Fig. 7b2. The sufficient depth of single track is defined as the depth of single track (d) that can be suitably melt with solid substrate. Furthermore, at higher layer thickness of 70 µm, and 100 µm, the single track with partial melting between powder bed and solid substrate or insufficient depth can be generated due to low thermal conductivity between metal powder bed layer and solid substrate (see in Fig. 7c2, d2). However, to obtain sufficient depth of single track at three different layer thickness of 30 µm, 70 µm, and 100 µm, the adjustment of energy input parameters such as laser power and scanning speed must be adjusted.

3.5 Influence of Adjustment of Energy Input Parameters on Forming Characteristics of Single Tracks

As previously mentioned in Sect. 3.4, the adjustment of energy input parameters such as the laser power and scanning speed is an efficient method to achieve sufficient

Table 3 The geometric dimensions of single track with different layer thickness

Case studies	P (W)	v (mm/s)	LED (J/mm)	L_t (µm)	w (µm)	d (µm)	Width-to-depth ratio
A1	200	1000	0.2	30	105	76	1.38
A2	200	1000	0.2	50	108	79	1.37
A3	200	1000	0.2	70	105	79	1.33
A4	200	1000	0.2	100	106	81	1.31

Table 4 The geometric dimension of single track in three conditions layer thickness of 30 μm, 70 μm, and 100 μm with different laser power and scanning speed

Case studies	P (W)	v (mm/s)	LED (J/mm)	L_t (μm)	w (μm)	d (μm)	Width-to-depth ratio
B1	125	1000	0.125	30	91	49	1.86
B2	200	1600	0.125	30	94	48	1.96
B3	250	1000	0.25	70	116	96	1.21
B4	200	800	0.25	70	120	95	1.26
B5	400	1000	0.4	100	127	150	0.85
B6	200	500	0.4	100	105	148	0.71

penetration depth of single tracks at three different layer thickness of 30 μm, 70 μm, and 100 μm. Nevertheless, when the laser power and scanning speed were adjusted for obtaining the sufficient depth of single track, they can influence on the single track characteristics such as geometric dimensions, melting modes, track shape, and track morphology. Consequently, in this section, the influence of adjustment of laser power and scanning speed on single track characteristics at three different layer thickness of 30 μm, 70 μm, and 100 μm was examined and discussed. Table 4 shows the geometric dimensions of single tracks at three conditions layer thickness of 30 μm, 70 μm, and 100 μm with different laser power and scanning speed. The numerical results indicated that the adjustment of energy input parameters including laser power and scanning speed can provide single track with sufficient penetration depth at three different layer thicknesses of 30 μm, 70 μm, and 100 μm. At layer thickness of 30 μm, the sufficient depth of single track was obtained when energy density was reduced. For example, the depth of single track reduced from 76 to 49 μm when laser power was decreased from 200 to 125 W (B1) and to 48 μm when the scanning speed was increased from 1000 to 1600 mm/s (B2). On the other hand, at layer thickness of 70 μm and 100 μm, the sufficient depth of single track in both cases can acquire with increasing of energy density. The single track depth at layer thickness of 70 μm and 100 μm increased from 79 μm and 81 μm to 96 μm and 150 μm when laser power was increased from 200 to 250 W (B3) and from 200 to 400 W (B5). When decreasing the scanning speed from 1000 to 800 mm/s (B4) and 500 mm/s (B6), the single track depth increased from 79 μm and 81 μm to 95 μm and 148 μm. Moreover, the single tracks width of case studies B1, B2, B3, B4, B5, and B6 were 91 μm, 94 μm, 116 μm, 120 μm, 127 μm, and 105 μm respectively. According to the results, it was found the adjustment of laser power and scanning speed have a more dominant effect on variation of single track width at layer thickness of 100 μm than layer thickness of 30 μm and 70 μm. This is because the higher layer thickness required more laser energy density to completely melt which results in process instability. The single track width is a key factor to impose the proper hatch spacing to fabricate effective final components with full dense and defects free.

In addition, the width-to-depth ratio of single track is a key parameter to define the melting modes. Generally, the melting modes in L-PBF process are mainly classified into three types including conduction mode (w/d ratio is over 1.5), transition mode (w/d ratio is between 1.0 and 1.5), and keyhole mode (w/d ratio is less than 1.0) [26, 47]. It was seen that the w/d ratio of single track of cases B1, B2, B3, B4, B5, and B6 were 1.86, 1.97, 1.21, 1.26, 0.85, and 0.71 consecutively as presented in Table 4. It can be summarized that the single tracks with conduction mode, which generally take places at low energy density and provide the wide and shallow molten pool shapes, were formed in case B1 and B2. When the medium energy density was determined at layer thickness of 70 μm case, the melting mode of single track changed from conduction mode to transition mode which produces more depth of penetration than conduction mode. Moreover, at the high layer thickness of 100 μm, the high energy density was applied as a result the changing of melting mode of single track from transition mode to keyhole mode. The keyhole mode largely produces narrow and deep melt pool shapes. A similar finding has been reported by a previous research study from He et al. [48]. In addition, Fig. 9 illustrates single tracks formation in three conditions layer thickness of 30 μm, 70 μm, and 100 μm with different laser power and scanning speed. The numerical results showed that the cross-section of single track in both cases of B1 (P = 125 W and v = 1000 mm/s) and B2 (P = 200 W and v = 1600 mm/s) at the layer thickness of 30 μm were narrow width, irregular shape, and shallow depth as displayed in Fig. 8a1, b1. As shown in Fig. 9a2, b2, it was found that single track with the continuous and regular size was formed in cases of B1 (P = 125 W and v = 1000 mm/s), whereas the single track with irregular and varying height can be generated in case B2 due to energy density and low interaction time (ratio of laser spot size to the scan velocity of laser source). As the layer thickness was 70 μm, the numerical results indicated that the single track with uniform tear-drop shape of molten pool and continuous track with regular size were generated in both cases B3 (P = 250 W and v = 1000 mm/s) and B4 (P = 200 W and v = 800 mm/s) (see in Fig. 9c1, c2, d1, d2. At higher layer thickness of 100 μm, the simulation results revealed that single track formation
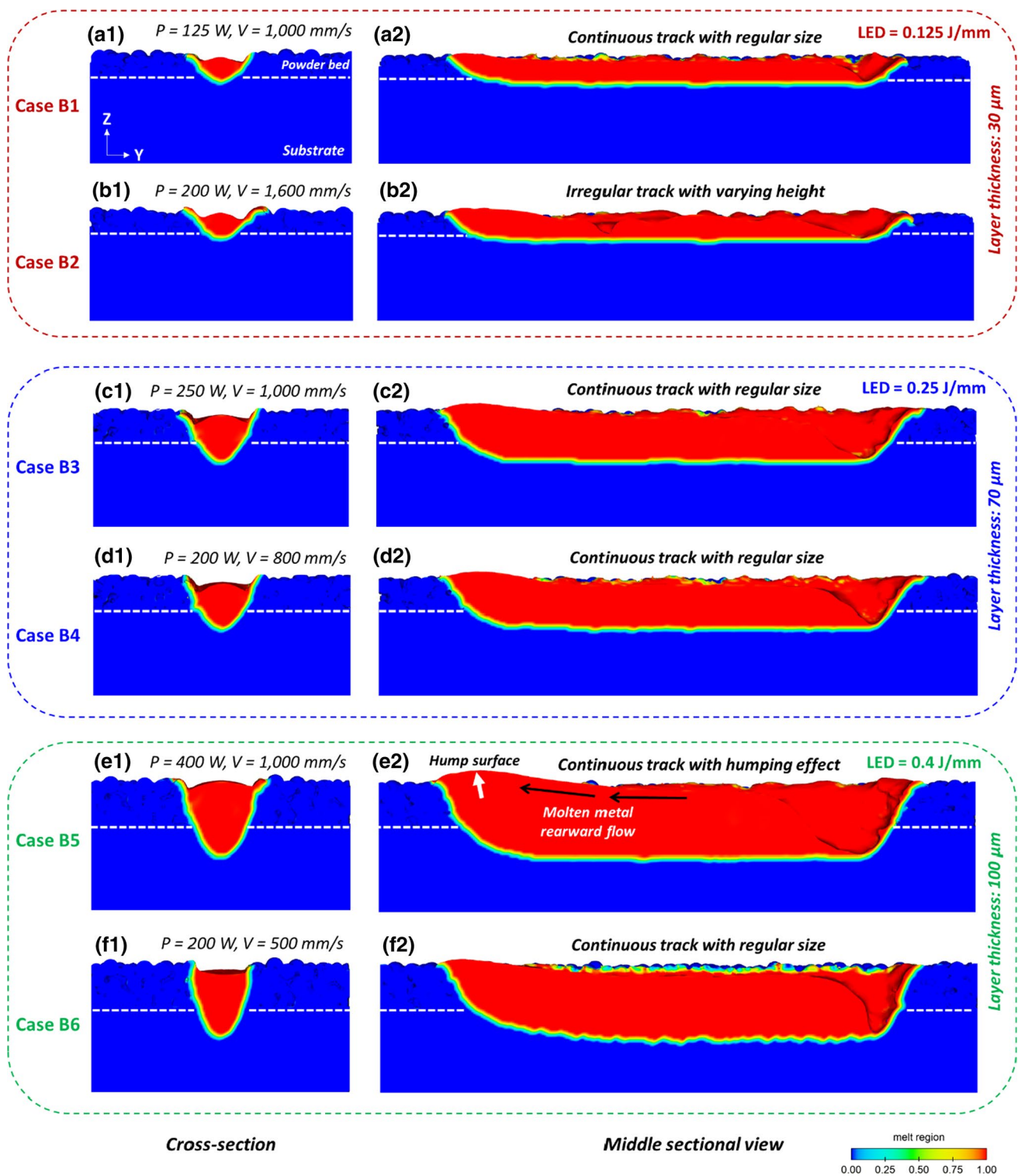
Fig. 9 Single tracks formation in three conditions layer thickness of 30 μm, 70 μm, and 100 μm with different laser power and scanning speed

in cases B5 and B6 were narrow track width and deep penetration depth (also known as keyhole mode). However, the continuous track with a humping effect can be formed in case of B5 (P = 400 W and v = 1000 mm/s) because the large

energy density was applied as shown in Fig. 9e2. The humping effect is caused by rearward flow of molten metal to agglomerate at hump surface. Similarly, the continuous track with a regular size was formed in case of B6 (P = 200 W and
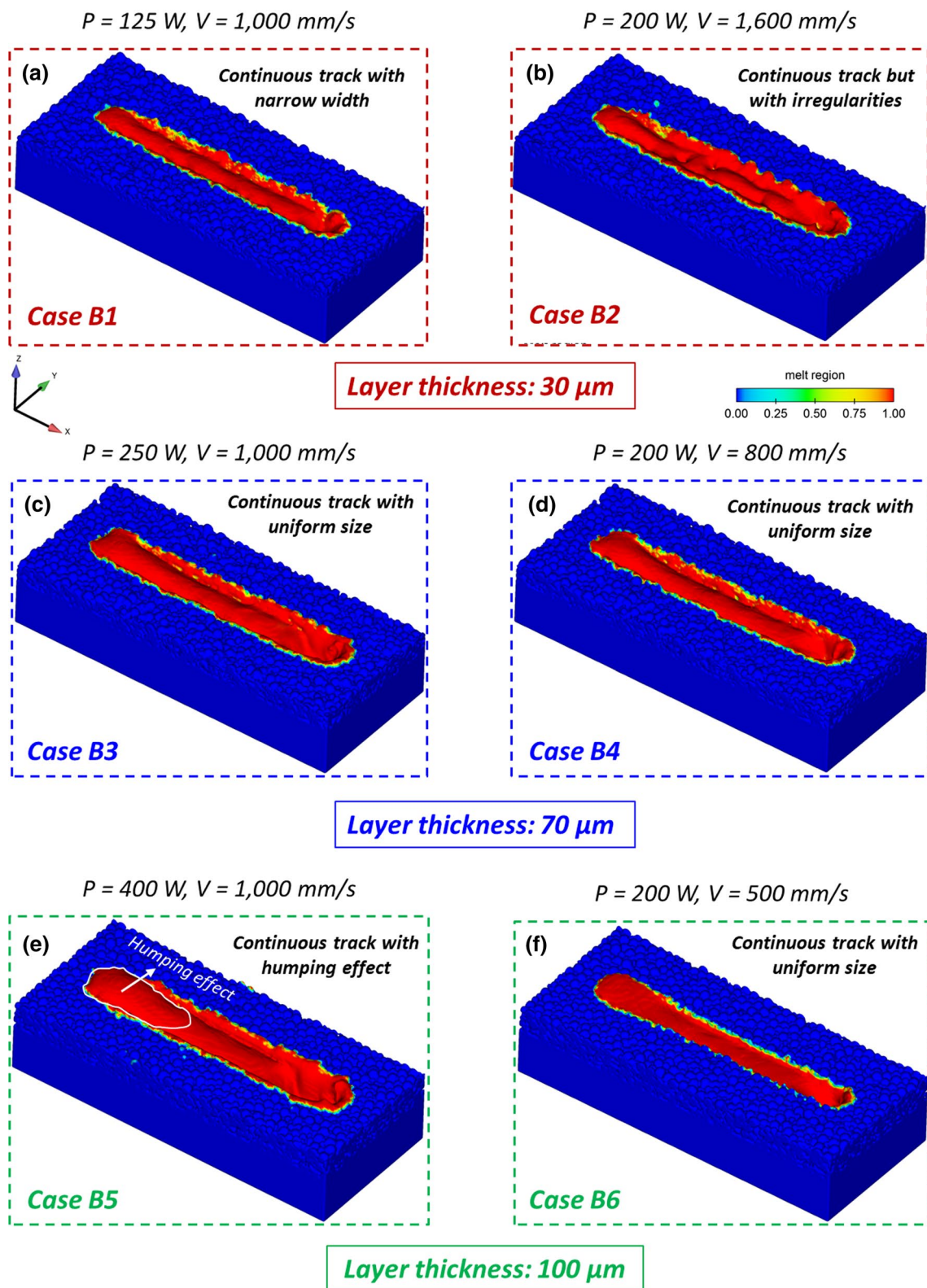
Fig. 10 Final solidified track morphology of single tracks in three conditions layer thickness of 30 μm, 70 μm, and 100 μm with different laser power and scanning speed

v = 500 mm/s) as exhibited in Fig. 9f2. Moreover, Fig. 10 exhibits final solidified track morphology of single track in three-layer thickness of 30 μm, 70 μm, and 100 μm with different laser power and scanning speed. The simulation results present that the continuous track with narrow width was originated in case of B1 and the continuous track with irregularities was formed in case of B2 as displayed in Fig. 10a, b. This is mainly because of the Plateau-Rayleigh capillary instability of liquid cylinder induced a surface tension effect and low interaction time between laser energy and powder bed. As illustrated in Fig. 10c, d, the final solidified track morphology of single track in both conditions of B3 and B4 has continuous track and regular size due to the sufficient heat energy. In addition, Fig. 10e, f exhibits the final solidified morphology of single track in cases of B5 and B6. It can be observed that the continuous track with hump surface can be formed in case of B5, while the solidified track morphology in case of B6 was continuous track with regular size. The result in this study that gained from numerical modelling revealed the layer thickness adjustment range between 50 and 70 μm with particle sizes used in this research can provide the single track with continuous, regular sizes and sufficient penetration depth when medium energy density is applied.

In addition, the AISI H13 components produced by L-PBF process are high crack susceptibility. The high cooling rate of solidified material results in large thermal stress, leading to high crack tendency [49]. Controlling of the cooling rate by adjustment process parameters is an effective method to decrease the thermal stress and the crack tendency during L-PBF. Thus, two cases with laser power and scanning speed of 200 W and 1000 mm/s (Case A4), and 400 W and 1000 mm/s (Case B5) were elected for additional investigation in this study. The local cooling rate data of solidified metal were obtained from probe A, which is attached at the middle of powder layer thickness. The numerical result revealed that when the energy density was increased from 0.2 J/mm (Case A4) to 0.4 J/mm (Case B5), the local cooling rates were reduced from 2.5×10^6 to 1.6×10^6 K/s for temperature ranges from 1657 to 1588 K and from 1.7×10^6 to 0.9×10^6 K/s for temperature ranges from 1588 to 900 K. This indicates that when the energy density was increased, the local cooling rate during L-PBF process was reduced and the crack tendency could be lower. The finding in this study is consistence with a previous research study of He et al. [48]. To further explore the thermal stress, the strain analysis, and the crack susceptibility of AISI H13 steel in L-PBF process, the linking between DEM-CFD model and mechanical FEM model, e.g., in the study of Chen and Yan [50], should be carried out in the future work.

4 Conclusions

In this current study, the Multiphysics modelling was implemented to examine the influence of layer thickness on thermal behavior, and single tracks characteristic during L-PBF process of AISI H13 tool steel. The influence of adjustment of energy input parameters on single tracks characteristic in various conditions of layer thickness were investigated. The findings of this research can be drawn as follows:

1. The DEM-CFD model can be implemented to investigate and predict the process parameters on complex physical phenomena in the L-PBF process such as thermal behavior, molten flow characteristic, and the molten pool evolution. Due to surface tension gradient at the melt pool surface, the molten metal rearward flowed from the hot spot zone at the laser center beam with high temperature to the solidified region with low temperature zone.

2. When the laser power of 200 W and scanning speed of 1000 mm/s, and LED of 0.2 J/mm were used, the single track with excessive penetration depth was formed with low layer thickness of 30 μm. When layer thickness was elevated from 30 to 50 μm, the single track with sufficient depth of penetration was generated. At layer thickness of 70 μm, and 100 μm, the single track with insufficient depth of penetration can be formed. In addition, the layer thickness has more influence on the single track depth than single track width. The lowest layer thickness of 30 μm presents the shallowest single tracks penetration depth due to high thermal conductivity between solid substrate and powder bed layer.

3. The single track with sufficient penetration depth at three different layer thicknesses of 30 μm, 70 μm, and 100 μm can be obtained when the energy input parameters were adjusted. It was discovered that the adjustment of laser power and scanning speed have dominant influence on single track width variation at layer thickness of 100 μm than layer thickness of 30 μm and 70 μm.

4. The depth of single track at layer thickness of 30 μm decreased around 28 μm when scanning speed increased from 1000 to 1600 mm/s, and 27 μm and the laser power was decreased from 200 to 125 W. Meanwhile, single track depth at high layer thickness of 70 μm increased around 19 μm when scanning speed decreased from 1000 to 800 mm/s and 20 μm when laser power increased from 200 to 250 W. At layer thickness of 100 μm, the depth of single track was increased around 67 μm when the scanning speed was reduced from 1000 to 500 mm/s, and 69 μm when laser power was increased from 200 to 400 W.

5. At layer thickness of 30 μm, the single track in both cases of P = 125 W and v = 1000 mm/s and P = 200 W and v = 1600 mm/s were narrow width, and irregular shape due to low energy density and low interaction time. As layer thickness of 70 μm, the single track with semicylindrical shape with regular size were generated in both cases of P = 250 W and v = 1000 mm/s and P = 200 W and v = 800 mm/s. At higher layer thickness of 100 μm, the continuous track with a humping effect was originated in case of P = 400 W and v = 1000 mm/s because the large energy density. Meanwhile, the continuous track with regular size was formed in case P = 200 W and v = 500 mm/s.

6. The single tracks with conduction mode were formed at low layer thickness of 30 μm because of low heat energy. At layer thickness of 70 μm, the melting mode of single track was transformed to transition mode because the medium energy density was used. Moreover, at the layer thickness of 100 μm, the melting mode of single track becomes keyhole mode due to the high energy density. Furthermore, when the high energy density was applied, the crack tendency could be decreased due to the lower local cooling rate during L-PBF process.

Nevertheless, the components in L-PBF process are generally built up additively layer-by-layer. Each powder layer bed is ordinarily fabricated in a track-by-track manner. Therefore, the future work should focus on the influence of process parameters on multi-tracks formation and defect formation such as porosity, thermal stress, and cracking to achieve the effective built component.

Declarations

Conflict of interest The authors declare no conflict of interest.

References

1. F. Véle, M. Ackermann, V. Bittner, J. Šafka, Materials **14**, 6052 (2021)
2. M. Narvan, K.S. Al-Rubaie, M. Elbestawi, Materials **12**, 2284 (2019)
3. J.J. Yan, D.L. Zheng, H.X. Li, X. Jia, J.F. Sun, Y.L. Li, M. Qian, M. Yan, J. Mater. Sci. **52**, 12476 (2017)
4. M. Narvan, A. Ghasemi, E. Fereiduni, S. Kendrish, M. Elbestawi, Mater. Design **204**, 109659 (2021)
5. J. Wang, S. Liu, Y. Fang, Z. He, Int. J. Adv. Manuf. Technol. **108**, 2453 (2020)
6. M. Mazur, M. Leary, M. McMillan, J. Elambasseril, M. Brandt, Rapid Prototyp. J. **22**, 504 (2016)
7. M. Abdel-latif, K. Abdel-Ghany, N. El-Mahallawy, T. Mattar, J. Mater. Eng. Perform. **30**, 8821 (2021)
8. B. Zhang, Y. Li, Q. Bai, Chin. J. Mech. Eng. **30**, 515 (2017)
9. M. Xia, D. Gu, G. Yu, D. Dai, H. Chen, Q. Shi, Int. J. Mach. Tools Manuf. **109**, 147 (2016)
10. S.M.H. Hojjatzadeh, N.D. Parab, W. Yan, Q. Guo, L. Xiong, C. Zhao, M. Qu, L.I. Escano, X. Xiao, K. Fezzaa, W. Everhart, T. Sun, L. Chen, Nat. Commun. **10**, 3088 (2019)
11. P. Bidare, A. Jiménez, H. Hassanin, K. Essa, Adv. Manuf. **10**, 175 (2021)
12. C.Y. Yap, C.K. Chua, Z.L. Dong, Z.H. Liu, D.Q. Zhang, L.E. Loh, S.L. Sing, Appl. Phys. Rev. **2**, 041101 (2015)
13. P. Ninpetch, P. Kowitwarangkul, S. Mahathanabodee, R. Tongsri, P. Ratanadecho, IOP Conf. Ser.: Mater. Sci. Eng. **526**, 012030 (2019)
14. P. Ninpetch, P. Kowitwarangkul, S. Mahathanabodee, P. Chalermkarnnon, P. Ratanadecho, AIP Conf Proc. **2279**, 050002 (2020)
15. A. Sola, A. Nouri, J. Adv. Manuf. Process. **1**, e10021 (2019)
16. P. Ninpetch, N. Teenok, P. Kowitwarangkul, S. Mahathanabodee, R. Tongsri, P. Ratanadecho, in *Proceedings of the IIWAP 2019*. The 8th n.a. Pac. IIW int. congr. Bangk. 20–22 March 2019, pp. 39–43
17. P.S. Cook, A.B. Murphy, Addit. Manuf. **31**, 100909 (2020)
18. M. Bayat, W. Dong, J. Thorborg, A.C. To, J.H. Hattel, Addit. Manuf. **47**, 102278 (2021)
19. H. Shipley, D. McDonnell, M. Culleton, R. Coull, R. Lupoi, G. O'Donnell, D. Trimble, Int. J. Mach. Tools Manuf. **128**, 1 (2018)
20. Z. Dong, W. Li, Q. Zhang, Y. Liu, J. Ge, X. Lin, J. Liang, J. Phys. D: Appl. Phys. **53**, 145501 (2020)
21. Z. Dong, Y. Liu, W. Wen, J. Ge, J. Liang, Materials **12**, 50 (2018)
22. P. Ninpetch, P. Kowitwarangkul, S. Mahathanabodee, P. Chalermkarnnon, P. Rattanadecho, Case Stud. Therm. Eng. **24**, 100860 (2021)
23. M. Markl, C. Körner, Annu. Rev. Mater. Res. **46**, 93 (2016)
24. W. Yan, Y. Qian, W. Ge, S. Lin, W.K. Liu, F. Lin, G.J. Wagner, Mater. Design **141**, 210 (2018)
25. B. Cheng, L. Loeber, H. Willeck, U. Hartel, C. Tuffile, J. Mater. Eng. Perform. **28**, 6565 (2019)
26. Q. Chen, Y. Zhao, S. Strayer, Y. Zhao, K. Aoyagi, Y. Koizumi, A. Chiba, W. Xiong, A.C. To, Addit. Manuf. **37**, 101642 (2021)
27. X. Chen, W. Mu, X. Xu, W. Liu, L. Huang, H. Li, Appl. Phys. A **127**, 586 (2021)
28. W. Ye, J. Bao, J. Lei, Y. Huang, Z. Li, P. Li, Y. Zhang, Met. Mater. Int. **28**, 282 (2022)
29. H.L. Wei, Y. Cao, W.H. Liao, T.T. Liu, Addit. Manuf. **34**, 101221 (2020)
30. L. Cao, Int. J. Heat Mass Transf. **141**, 1036 (2019)
31. C. Panwisawas, C. Qiu, M.J. Anderson, Y. Sovani, R.P. Turner, M.M. Attallah, J.W. Brooks, H.C. Basoalto, Comput. Mater. Sci. **126**, 479 (2017)
32. Y.-C. Wu, C.-H. San, C.-H. Chang, H.-J. Lin, R. Marwan, S. Baba, W.-S. Hwang, J. Mater. Process. Tech. **254**, 72 (2018)
33. X. Shi, C. Yan, W. Feng, Y. Zhang, Z. Leng, Opt. Laser Technol. **132**, 106471 (2020)
34. X. Shi, S. Ma, C. Liu, C. Chen, Q. Wu, X. Chen, J. Lu, Materials **9**, 975 (2016)
35. C. Qiu, C. Panwisawas, M. Ward, H.C. Basoalto, J.W. Brooks, M.M. Attallah, Acta Mater. **96**, 72 (2015)
36. Y. Guo, L. Jia, B. Kong, N. Wang, H. Zhang, Chin. J. Aeronaut. **31**, 860 (2018)

37. B. Cheng, X. Li, C. Tuffile, A. Ilin, H. Willeck, U. Hartel, in *Proceedings of the 29th Annual International Solid Freeform Fabrication Symposium – An Additive Manufacturing Conference*, ed. by D.L. Bourell, J.J. Beaman, Ri.H. Crawford, S. Fish, C.C. Seepersad. n.a. 13–15 August 2018, pp. 1887–1902

38. Y.S. Lee, W. Zhang, Addit. Manuf. **12**, 178 (2016)

39. Y. Tian, L. Yang, D. Zhao, Y. Huang, J. Pan, J. Manuf. Process. **58**, 964 (2020)

40. W. Ge, J.Y.H. Fuh, S.J. Na, J. Manuf. Process. **62**, 646 (2021)

41. Z. Ren, D.Z. Zhang, G. Fu, J. Jiang, M. Zhao, Mater. Design **207**, 109857 (2021)

42. Y.-C. Wu, W.-S. Hwang, C.-H. San, C.-H. Chang, H.-J. Lin, Int. J. Mater. Form. **11**, 807 (2018)

43. C. Wu, M.Q. Zafar, H. Zhao, Y. Wang, C. Schöler, C. Heinigk, M. Nießen, W. Schulz, Addit. Manuf. **47**, 102274 (2021)

44. M. Bayat, V.K. Nadimpalli, F.G. Biondani, S. Jafarzadeh, J. Thorborg, N.S. Tiedje, G. Bissacco, D.B. Pedersen, J.H. Hattel, Addit. Manuf. **43**, 102021 (2021)

45. P. Promoppatum, S.-C. Yao, P.C. Pistorius, A.D. Rollett, P.J. Coutts, F. Lia, R. Martukanitz, Prog. Addit. Manuf. **3**, 15 (2018)

46. L. Cao, Metall. Mater. Trans. A **52**, 211 (2021)

47. Q. Guo, C. Zhao, M. Qu, L. Xiong, L.I. Escano, S.M.H. Hojjatzadeh, N.D. Parab, K. Fezzaa, W. Everhart, T. Sun, L. Chen, Addit. Manuf. **28**, 600 (2019)

48. Y. He, M. Zhong, J. Beuth, B. Webler, J. Mater. Process. Tech. **286**, 116802 (2020)

49. Y. Li, D. Gu, Mater. Design **63**, 856 (2014)

50. F. Chen, W. Yan, Mater. Design **196**, 109185 (2020)